

University of Nebraska - Lincoln

DigitalCommons@University of Nebraska - Lincoln

Faculty Publications, Department of Physics
and Astronomy

Research Papers in Physics and Astronomy

2023

Anisotropic optical and magnetic response in self-assembled TiN-CoFe₂ nanocomposites

Jiawei Song

Di Zhang

Ping Lu

Haohan Wang

X. S. Xu

See next page for additional authors

Follow this and additional works at: <https://digitalcommons.unl.edu/physicsfacpub>



Part of the [Physics Commons](#)

This Article is brought to you for free and open access by the Research Papers in Physics and Astronomy at DigitalCommons@University of Nebraska - Lincoln. It has been accepted for inclusion in Faculty Publications, Department of Physics and Astronomy by an authorized administrator of DigitalCommons@University of Nebraska - Lincoln.

Authors

Jiawei Song, Di Zhang, Ping Lu, Haohan Wang, X. S. Xu, Melissa L. Meyerson, Samantha G. Rosenberg, Julia Deitz, Juncheng Liu, Xuejing Wang, and Xinghang Zhang

1 **Anisotropic optical and magnetic response in self-assembled TiN-CoFe₂ nanocomposites**

2 Jiawei Song¹, Di Zhang^{1,2}, Ping Lu³, Haohan Wang⁴, Xiaoshan Xu⁴, Melissa L. Meyerson³,

3 Samantha G. Rosenberg³, Julia Deitz³, Juncheng Liu¹, Xuejing Wang², Xinghang Zhang¹,

4 Haiyan Wang^{1,5*}

5

6 ¹*School of Materials Engineering, Purdue University, West Lafayette, 47907, USA*

7 ²*Center for Integrated Nanotechnologies (CINT), Los Alamos National Laboratory, Los*
8 *Alamos, NM 87545, USA*

9 ³*Sandia National Laboratories, Albuquerque, NM 87185, USA*

10 ⁴*Department of Physics and Astronomy, University of Nebraska-Lincoln, Lincoln, NE 68588,*
11 *USA*

12 ⁵*School of Electrical and Computer Engineering, Purdue University, West Lafayette, 47907,*
13 *USA*

14

15 *Address correspondence to: hwang00@purdue.edu (Haiyan Wang)

16 **Abstract:**

17 Transition metal nitrides (e.g., TiN) have shown tremendous promise in optical metamaterials
18 for nanophotonic devices due to their plasmonic properties comparable to noble metals and
19 superior high temperature stability. Vertically aligned nanocomposites (VANs) offer a great
20 platform for combining two dissimilar functional materials with a one-step deposition
21 technique toward multifunctionality integration and strong structural/property anisotropy. Here
22 we report a two-phase nanocomposite design combining ferromagnetic CoFe₂ nanosheets in
23 the plasmonic TiN matrix as a new hybrid plasmonic metamaterial. The hybrid metamaterials
24 exhibit obvious anisotropic optical and magnetic responses, as well as a pronounced magneto-
25 optical coupling response evidenced by MOKE measurement, owing to the novel vertically
26 aligned structure. This work demonstrates a new TiN-based metamaterial with anisotropic
27 properties and multi-functionality towards optical switchable spintronics, magnetic sensors and
28 integrated optics.

29

30 **Key Words: Vertically aligned nanocomposites; Tunable microstructure; Hyperbolic**
31 **metamaterial; Magnetic anisotropy; Magneto-optical coupling**

32
33
34
35
36
37
38
39
40
41
42
43
44
45
46
47
48
49
50
51
52
53
54

55 **Introduction**

56 Optical metamaterials consist of artificially designed nanostructured materials which
57 generate unique optical properties that are not exhibited in natural materials. These novel
58 optical properties, including negative refractive index[1,2], near-zero-index[3], and hyperbolic
59 dispersion[4,5], originate from the confinement of light propagation in nanostructured
60 materials. Noble metals (e.g., Au and Ag) are widely used in forming nanostructured plasmonic
61 metamaterials due to their strong surface plasmon resonance. However, plasmonic metals
62 exhibit high optical loss in the visible to near-infrared (vis-NIR) region due to inter-band and
63 intra-band transitions[6]. In addition, other challenges in terms of fabrication and integration,
64 as well as permittivity tuning of plasmonic metamaterials, greatly hinder their performances
65 and applications[7]. Therefore, seeking alternative plasmonic materials is necessary to
66 overcome these drawbacks. Transition metal nitrides (e.g. TiN, TaN, ZrN, etc) are promising
67 candidates for plasmonic applications because of their metallic response in most optical
68 wavelengths and high structural stability. Tailoring stoichiometry in nitrides allows tuning of
69 optical properties easily[8]. Considering the fabrication and integration challenges of metals,
70 transition metal nitrides are compatible with the complementary metal-oxide-semiconductor
71 (CMOS) process and can be easily integrated on various substrates (e.g., MgO, STO, Si,
72 sapphire)[9,10]. Besides, the high mechanical strength and high melting temperature enable
73 them to be promising materials for future high temperature plasmonic applications[11,12].

74 With the development of nanofabrication techniques, various nanostructured nitrides
75 have been demonstrated for plasmonic applications, e.g., periodic array of TiN
76 nanoparticles[13], nanoantennas[14], nanotrenches[15], and nanorings[16]. The integration of
77 TiN with dielectric materials (e.g., AlN, MgO) into a multilayer structure has been explored
78 exhibiting hyperbolic dispersion[17,18]. However, most of these TiN-based metamaterials rely
79 on high-cost fabrication techniques, including e-beam lithography and focused ion-beam

80 process. Compared to the conventional fabrication methods, a cost-effective self-assembly
81 approach to growing hybrid materials into a vertically aligned nanocomposite (VANs) form
82 has recently attracted tremendous interest. Multiple two-phase nitride-metal
83 nanocomposites[19–21], such as TaN-Au, TiN-Au, and TiN-Ag, have been successfully
84 demonstrated in VANs with enhanced surface plasmon resonance and nonlinear optical
85 responses. Taking advantage of these simple self-assembly VAN platforms, other nitride-based
86 nanostructures can be further derived by additional processes. For example, TiN nanohole
87 arrays have been achieved by selectively etching away the Au nanopillars from TiN-Au
88 VANs[22], and a 3D plasmonic framework is formed by alternating TiN-Au and TaN-Au
89 layers[23]. Most of the prior demonstrations have been focusing on nitride-metal[19–21] or
90 oxide-metal[24–29] systems as hybrid metamaterials.

91 Another opportunity brought by the designs of VANs is integrating different
92 functionalities in one material system. Functional materials are a large material family with a
93 wide selection of properties, such as plasmonic (e.g., Au[7]), superconductivity (e.g.,
94 $\text{YBa}_2\text{Cu}_3\text{O}_{7-\delta}$ [30]), ferromagnetic (e.g., CoFe_2O_4 [31], MnFe_2O_4 [32], CoFe_2 [33]),
95 ferroelectricity (e.g., BaTiO_3 [34]), and multiferroicity (e.g., BiFeO_3 [35]) etc.
96 Multifunctionality, as well as coupling effects, have been demonstrated in oxide-based VANs,
97 such as magneto-electric coupling [36–38] and magneto-optic coupling effects [25,39,40]. On
98 the other hand, most of the previous nitride-based VANs focus on incorporating plasmonic
99 metal nanopillars towards optical tunability. Therefore, incorporating a secondary functional
100 phase into the nitride matrix could enormously broaden the nitride VAN designs with other
101 functionality. However, such nitride-based nanocomposite demonstration is very limited due
102 to the challenges in material design incompatibility and differences in growth parameters
103 required for the different phases.

104 In this work, we report a new hybrid metamaterial system of TiN-based nanocomposite
105 with ferromagnetic CoFe₂ in the VAN form with strong anisotropic optical and magnetic
106 properties. Here, ferromagnetic CoFe₂ nanopillars were formed by reducing CoFe₂O₄ in the
107 target material during the high vacuum condition required by TiN growth. The TiN-CoFe₂
108 VANs are expected to exhibit optical and magnetic anisotropy as well as potential magneto-
109 optical coupling. Laser frequency is varied to be 2 Hz and 10 Hz to effectively tune the
110 dimension of CoFe₂ pillars. This demonstration shows the potential of designing new nitride-
111 based VAN systems with multifunctionalities, property coupling, as well as effective property
112 tunability.

113

114 **Results and Discussion**

115 The microstructure of TiN-CoFe₂ nanocomposites thin films was first characterized by
116 XRD analysis using θ -2 θ scans as shown in Fig. S1. An obvious out-of-plane of TiN (002),
117 and MgO (002) can be clearly observed in the 2 Hz and 10 Hz deposited samples. The peak at
118 the right side of the substrate MgO peak ($2\theta=43.254^\circ$) can be identified as CoFe₂ (011). The
119 out-of-plane d-spacing of CoFe₂ (011) was determined by 2.09 Å which is in 3.5% strain
120 compared to its bulk value 2.02 Å. To reveal the detailed chemical distribution and 2-phase
121 morphology in the system, a scanning transmission electron microscopy (STEM) analysis
122 along with energy-dispersive X-ray spectroscopy (EDS) mapping was conducted on the
123 samples in both cross-section and plan-view directions. As shown in the cross-sectional (Fig.
124 1b) and plan-view (Fig. 1d) STEM images, the two-phase nanocomposites exhibit a nanosheet-
125 in-matrix structure. In the STEM images taken using the high angle annular dark field
126 (HAADF) detector, the contrast is proportional to the atomic number (i.e., $\sim Z^{1.7}$) [41–43].
127 Therefore, the brighter nanosheet region is related to the higher atomic number of Co ($Z = 26$)
128 and Fe ($Z = 27$), compared to TiN (averaged $Z = 14.5$). The EDS maps in Fig. 1e further

129 confirm the formation of ultrathin nanosheets made of Co and Fe, perpendicularly embedded
130 in the TiN matrix. Furthermore, two high-resolution STEM images with higher magnifications
131 from one of the nanosheet regions from the cross-sectional and plan-view images are shown in
132 Fig. 1c and Fig. 1f respectively. Based on the lattices measured and symmetry identified, it
133 determines that the nanosheets in the view area are metallic CoFe_2 with a body-center-cubic
134 (bcc) structure and a lattice constant of 2.86 Å, and furthermore form an epitaxy with the TiN
135 matrix.

136 Of additional interest is that the “pillars” shape is rectangular in-plane (shown in plan-
137 view images Fig 1d-f), i.e., thin sheet-like nanopillars, which is very different from the circular
138 shape in the previously reported TiN-based VAN structures [20,21,44,45]. To understand the
139 mechanism behind the nanosheet formation, we also investigated the strain states around the
140 nanosheet using geometric phase analysis (GPA) based on a high-resolution STEM
141 (HRSTEM) image. The color maps, ϵ_{yy} (Fig. 1g) and ϵ_{xx} (Fig. 1f), are generated with x
142 direction perpendicular to the plate, and y direction parallel to the plate. The strain maps are
143 calculated with respect to the lattice plane spacings in the TiN matrix, with a displayed strain
144 ranging from -30% to +30%. A high compressive strain exists in the nanosheet area (i.e., white
145 contrast area) in the ϵ_{xx} mapping, but a relatively neutral strain (i.e., green contrast) in the
146 nanosheet area in the ϵ_{yy} . This suggests the higher strain in the x-direction (normal to plate of
147 the pillars) than that in the y-direction (parallel to plate of the pillars). This anisotropic in-plane
148 strain can also explain the anisotropic rectangular shapes of the nanosheets observed which is
149 to minimize the overall strain energy in the entire system, i.e., the longer edges present minimal
150 strain (lattice-matched with the TiN matrix), while the shorter edges present large compressive
151 strain to the TiN matrix. The anisotropic in-plane strain can also be confirmed by the intensity
152 line profiles (Fig. S2 b1-b4) extracted from the plan-view HRSTEM image (Fig. 1f). Along the
153 x-direction, the d-spacing of TiN and CoFe_2 phase are 2.12 Å and 1.43 Å separately which

154 corresponds with a relatively large lattice strain of 32%. The lattice strain is relatively small
155 along the y-direction because the two phases have comparable d-spacing (2.12 Å for TiN and
156 2.02 Å for CoFe₂). The in-plane orientation relationships can be identified as
157 CoFe₂[100]//TiN[200] and CoFe₂[011]//TiN[020].

158 To further investigate the chemical compositions of the TiN-CoFe₂ nanocomposites,
159 we conducted X-ray photoelectron spectroscopy (XPS) depth-profiling measurements by
160 alternately sputtering material off the surface and measuring the freshly exposed surface with
161 XPS. Before any sputtering, the surface shows that Fe, Ti, and Co are mostly in the oxide phase,
162 which is expected for films having been exposed to air. It is interesting to note that, as shown
163 in Fig. S3 c-d, after sputtering off the adventitious carbon and oxygen the metallic CoFe₂ is
164 revealed to be the dominant species. However, it is noted that the small oxygen peaks remain
165 below the top surface of the nanocomposite sample, which suggests the Co-O and Fe-O bonds
166 remain in the nanocomposites. This is likely due to Co and Fe bonding to oxygen atoms at the
167 nanosheet/matrix interfaces. The XPS shows the co-existence of TiO_xN_y and TiN peaks in Ti
168 2p spectra in the matrix, indicating minor oxidation of TiN.

169 The microstructure tunability was realized by tuning laser frequency from 2 Hz to 10
170 Hz as shown in Fig. 2b and Fig. 2d. Since the CoFe₂ nanosheets have a rectangular-shape cross
171 area, we analyzed the length distribution of the short edge and long edge respectively and
172 plotted them in Fig. 2c and Fig. 2f. As laser frequency increases, the dimension of CoFe₂
173 nanosheets decreases significantly. The average dimension of CoFe₂ sheets in the 2 Hz sample
174 is 7.39nm × 30.61nm, while it decreases to 3.14nm × 16.73nm by increasing the laser
175 frequency to 10 Hz. The tunability in dimension can be explained by the shorter adatoms
176 diffusion time during the deposition process with higher laser frequency. Besides laser
177 frequency, the temperature-dependent study provides another approach to effectively tune the
178 microstructure of TiN-CoFe₂ thin films (Fig. S4). Clearly, as the temperature increases from

179 500 °C to 700 °C, the CoFe₂ nanosheet dimensions increase from 1.45nm × 4.69nm to
180 7.39nm × 30.61nm.

181

182 The optical properties of the two-phase TiN-CoFe₂ nanocomposites were characterized
183 by spectroscopic ellipsometry. The ellipsometry data ψ and Δ were collected on both 2 Hz and
184 10 Hz TiN-CoFe₂ films, and compared with two reference samples, i.e., a pure TiN film and a
185 pure CoFe₂O₄ film. It is noted the reference single phase CoFe₂O₄ film was grown under
186 vacuum condition, which may also have partial reduction and form CoFe₂ phase. To retrieve
187 the dielectric permittivity, the data were fitted by applying general oscillator models. The real
188 part of the dielectric permittivity (Fig. 3a) confirms pure TiN is metallic ($\epsilon' < 0$) and pure
189 CoFe₂O₄ film is dielectric ($\epsilon' > 0$) for most wavelengths. Due to the anisotropic nature of two-
190 phase VAN films, the permittivity of VAN films is fitted and plotted along out-of-plane (ϵ_{\perp})
191 in solid lines and in-plane (ϵ_{\parallel}) in dashed lines, respectively. It is clear that the out-of-plane real
192 permittivity(ϵ_{\perp}) of both 2 Hz and 10 Hz samples is positive but very close to 0 throughout all
193 the measured wavelengths, while in-plane real permittivity (ϵ_{\parallel}) exhibits negative values
194 throughout. The opposite sign in optical permittivity demonstrates a large Type-II hyperbolic
195 dispersion regime (i.e., $\epsilon_{\perp} > 0$ and $\epsilon_{\parallel} < 0$) as the shaded area in Fig. 3a). Considering the
196 metallic CoFe₂, it is possible that the CoFe₂ phase could also contribute to the overall negative
197 permittivity in-plane. The remaining small amount of oxygen containing phase at the surface
198 and partial oxidation of TiN matrix near interface could both contribute to the overall positive
199 permittivity out-of-plane. Note that the 10 Hz sample shows a larger negative value of ϵ'_{\parallel}
200 compared to the 2 Hz one, suggesting that higher density of the nanopillars and more vertical
201 interfaces present stronger optical anisotropy in the system. Fig. 3b plots the imaginary
202 permittivity as a function of wavelength. Both the 2 Hz and 10 Hz samples show small optical

203 losses along the out-of-plane direction because of their more dielectric nature compared to the
204 TiN alone.

205

206 To further study the magnetic behavior of TiN-CoFe₂ nanocomposites, magnetization
207 (M) vs. magnetic field (H) was measured in in-plane and out-of-plane directions at room
208 temperature using Quantum Design SQUID-VSM. As shown in Fig. 4a, the out-of-plane
209 hysteresis loops of 2Hz sample exhibits a saturation magnetization $M_{s\perp} = 329 \text{ emu/cm}^3$,
210 and coercivity $H_{c\perp} = 1235 \text{ Oe}$, while the magnetization and coercivity along in-plane
211 direction are only $M_{s\parallel} = 257 \text{ emu/cm}^3$ and $H_{c\parallel} = 708 \text{ Oe}$ respectively. The wider out-of-
212 plane loop suggests a strong magnetic anisotropy with an out-of-plane easy axis, which result
213 from the perpendicular elongated shape of CoFe₂(O) nanosheets. The magnetic behavior of
214 10Hz sample shows a similar trend, with smaller coercivity $H_{c\perp} = 771 \text{ Oe}$ and $H_{c\parallel} = 367 \text{ Oe}$
215 (Fig. 4b). This can be explained by the smaller dimension of CoFe₂ nanosheets. Considering
216 the possibility of coupling effect between plasmonic TiN and ferromagnetic CoFe₂, it is worth
217 to study their magneto-optical (MO) coupling properties. Magneto Optic Kerr Effect (MOKE)
218 measurements were conducted on both 2Hz and 10Hz samples under room temperature and
219 the results are plotted in Fig. 4c-f. Polar MOKE was measured with a normal incident laser (
220 $\lambda = 632.8 \text{ nm}$) and out-of-plane magnetic field, while a 30° laser and in-plane magnetic field
221 were induced in longitudinal MOKE configuration. The obtained MOKE M-H loops indicate
222 that a magneto-optical (MO) coupling effect presents in both two samples. The results show a
223 similar trend with that characterized by VSM, i.e., very strong perpendicular magnetic
224 anisotropy and tunable coercivity comparing the 2Hz and 10Hz samples. Furthermore, the
225 10Hz sample shows a larger Kerr rotation signal compared to the 2Hz sample, in both out-of-
226 plane and in-plane directions. This can be explained by the enhanced coupling introduced by

227 the higher density of TiN-CoFe₂ interfaces in the 10Hz sample compared to that in the 2Hz
228 sample.

229

230 The overall characteristics of the new TiN-CoFe₂ hybrid metamaterial are the
231 anisotropic CoFe₂ nanosheets formed in the TiN matrix, high epitaxial film quality, anisotropic
232 optical and magnetic properties, as well as unique magneto-optical coupling properties.
233 Compared to the TiN-Au, TiN-Ag, and TaN-Au systems previously demonstrated[19–21],
234 TiN-CoFe₂ opens up the potential of highly anisotropic metamaterials designs, i.e., non-
235 magnetic vs. strong magnetic. The unique magneto-optical coupling demonstrated at the TiN
236 and CoFe₂ interfaces also presents opportunities in future designs of optical switchable
237 spintronic devices and magnetic data storage devices. One of the major challenges is the
238 interdiffusion between the oxide and the nitride in the system and the resultant reduction of the
239 oxide phase. Selecting more stable oxides and minimizing interdiffusion by controlling the
240 growth conditions will be critical for future exploration of nitride-oxide hybrid systems.
241 Additional tunability can be achieved by other material combinations, novel three-phase
242 system designs, and multilayer stacks of nitride-oxide VAN with other systems for integrated
243 functionalities.

244

245 **Conclusion**

246 In summary, we have demonstrated self-assembled TiN-CoFe₂ nanocomposite thin
247 films by using the one-step PLD technique. Microstructure characterizations by STEM and
248 XPS show ultrathin nanosheets with metallic CoFe₂ phase growing vertically aligned in the
249 TiN matrix. Both the deposition frequency study (2Hz, 10Hz) and temperature-dependent
250 studies suggest effective tunability in the microstructure of the secondary phase as well as the
251 resultant properties. Ellipsometry measurements reveal that the samples exhibit a Type-II

252 hyperbolic dispersion in most optical wavelengths considering the highly anisotropic
253 morphology of the TiN matrix, vertically aligned
254 oxides between the TiN matrix and the CoFe₂ nanosheets. The magnetic hysteresis loops reveal
255 obvious magnetic anisotropy owing to the highly aligned CoFe₂ nanosheets. The well-
256 integrated plasmonic and ferromagnetic materials in the hybrid system enable a strong
257 magneto-optical coupling effect at the pillar-matrix interfaces. This new nitride-based
258 metamaterial design demonstrated in this study may provide new routes for processing of
259 nitride-metal based nanocomposites with enhanced anisotropic structural and physical
260 properties, towards future photonic devices and optical switchable spintronic devices.

262 **Acknowledgement**

263 This work was supported by the U.S. National Science Foundation DMR-2016453 and DMR-
264 1565822 (VAN thin film growth and High-resolution STEM work, respectively). The work at
265 University of Nebraska was supported by the U.S. National Science Foundation through
266 EPSCoR RII Track-1: Emergent Quantum Materials and Technologies (EQUATE), Award No.
267 OIA-2044049. The work at Los Alamos National Laboratory was supported by the NNSA's
268 Laboratory Directed Research and Development Program and was performed, in part, at the
269 Center for Integrated Nanotechnologies, an Office of Science User Facility operated for the
270 U.S. Department of Energy Office of Science. Los Alamos National Laboratory, an affirmative
271 action equal opportunity employer, is managed by Triad National Security, LLC for the U.S.
272 Department of Energy's NNSA, under contract 89233218CNA000001. The microscopy work
273 was partially supported by the Laboratory Directed Research and Development program at
274 Sandia National Laboratories. Sandia National Laboratories is a multi-mission laboratory
275 managed and operated by National Technology and Engineering Solutions of Sandia, LLC., a
276 wholly owned subsidiary of Honeywell International, Inc., for the U.S. Department of Energy's

277 National Nuclear Security Administration under Contract No. DE-NA0003525. This paper
278 describes objective technical results and analysis. Any subjective views or opinions that might
279 be expressed in the paper do not necessarily represent the views of the U.S. Department of
280 Energy or the United States Government.

281

282 **Methods**

283

284 **Thin film growth**

285 The TiN-CoFe₂O₄ target consists of pie-shape CoFe₂O₄ and TiN targets. The
286 nanocomposite thin films were deposited on MgO (001) substrates in Neocera pulsed laser
287 deposition chamber with a KrF excimer laser (Lambda Physik Compex Pro 205, $\lambda = 248$ nm).
288 The substrates were heated and maintained at 700 °C during deposition and a high vacuum
289 condition (2.0×10^{-6} mbar) was kept during deposition and cooling process.

290 **Structural characterization**

291 X-ray Diffraction

292 The $\theta/2\theta$ XRD scans were measured by a Panalytical X'Pert X-ray diffractometer with
293 a Cu K α 1 radiation source ($\lambda = 0.15406$ nm).

294 Transmission Electron Microscopy

295 Transmission electron microscopy (TEM) and scanning transmission electron
296 microscopy (STEM) (under a high angle annular dark field mode (HAADF)) were taken on a
297 Thermo Fisher Scientific (FEI) Talos F200X system with a point-to-point resolution of 1.6 Å.
298 High-resolution STEM images were collected on an aberration-corrected FEI Titan microscope
299 equipped with a high-brightness Schottky field emission electron source operated at 300 kV.
300 A FEI TitanTM G2 80-200 STEM with a Cs probe corrector and ChemiSTEMTM technology
301 (X-FEGTM and SuperXTM EDS with four windowless silicon drift detectors) operated at 200

302 kV was used for HAADF-STEM imaging and EDS analysis. A Digital Micrograph plug-in
303 (DM 1.8.3 package, HRTEM Research Inc.) was used for geometric phase analysis (GPA).
304 The cross-sectional TEM samples were prepared by a standard procedure, including manual
305 grinding, polishing, dimpling and a final ion milling step (PIPS 695 precision ion polishing
306 system, Gatan Inc.).

307 X-ray Photoelectron Spectroscopy

308 XPS was performed using a Kratos Axis Supra XPS system with a monochromatic Al
309 K α X-ray source. An initial spectrum was taken of the surface of every sample before a depth
310 profile for 40 steps was performed with a gas cluster ion sputtering system at 10 keV 1000
311 clusters for 60 seconds with an incidence angle of 40° with respect to the horizontal direction.
312 The size of the analyzed area was 110 μm x 110 μm while the sputtered size was 2 mm x 2 mm
313 (rastered). Base pressure during analysis was 1.2×10^{-9} torr and the electron emission angle was
314 at 54.7° with an active charge neutralizer. XPS data was analyzed using CasaXPS software
315 with the Kratos relative sensitivity factors set to F 1s at 1. The O 1s signal at 530.6 eV (MgO)
316 was used as an internal reference for peak positions for all samples.

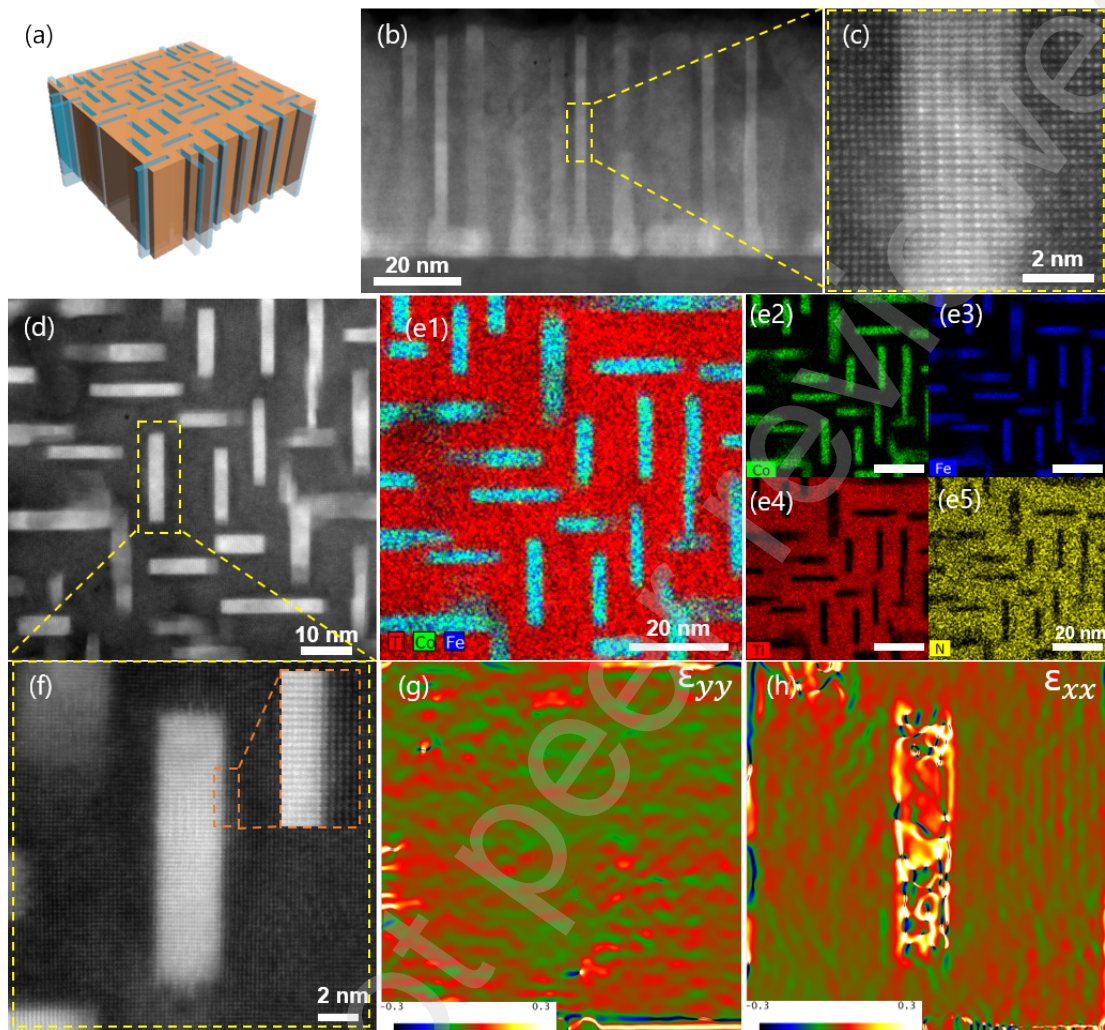
317 **Optical characterization**

318 Spectroscopic ellipsometry measurements were carried out with a spectroscopic
319 ellipsometer (J.A. Woollam RC₂) with variable angles (55°, 65°, and 75°) and spectrum range
320 from 210 nm to 2500 nm. The real and imaginary part of permittivity were obtained by fitting
321 ellipsometer parameters ψ (Ψ) and Δ with Gen-Osc model in CompleteEASE software.
322 Transmittance spectra were measured on UV–vis-NIR absorption spectrophotometer (Perkin
323 Elmer Lambda 1050).

324 **Magnetic Characterization**

325 The magnetic hysteresis loops were measured by a Quantum Design MPMS-3 SQUID
326 Magnetometer with vibrating sample magnetometer (VSM) mode. The magneto-optic Kerr

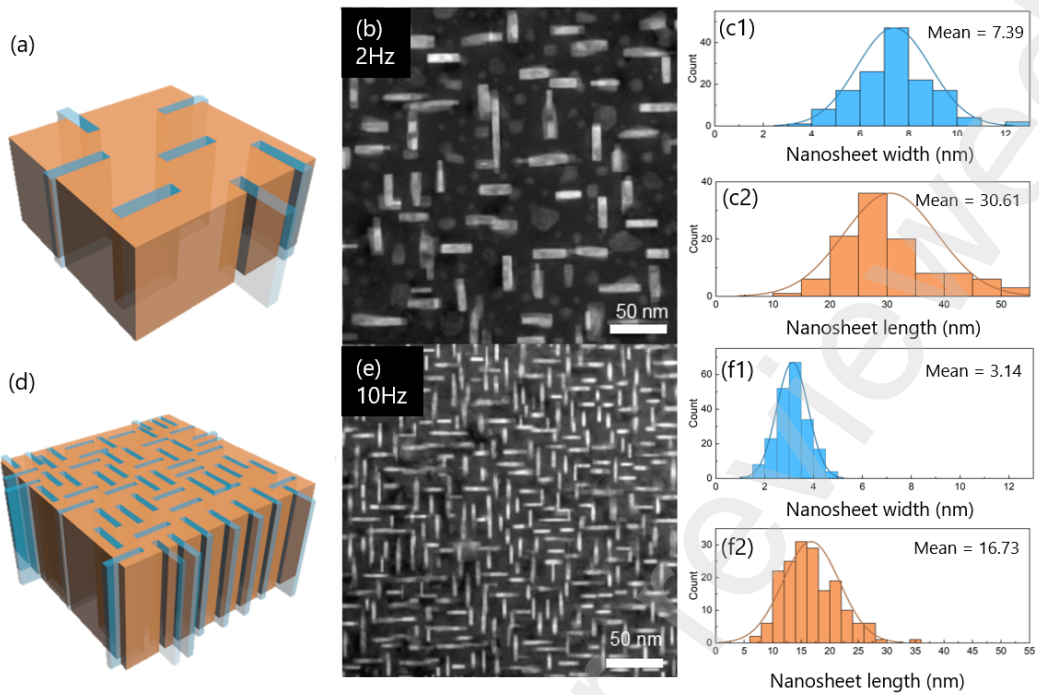
327 effect (MOKE) measurements were carried out by a home-built system equipped with a
328 photoelastic modulator with two polar (P) and longitudinal (L) configurations. A laser with a
329 wavelength of 632 nm was applied as a source light and the magnetic field was in the range of
330 -3500 Oe to 3500 Oe for P-MOKE and -7000 Oe to 7000 Oe for L-MOKE separately.



332

333 **Fig. 1 | Microstructure of TiN-CoFe₂ nanocomposite thin film.** (a) Schematic drawing of
 334 TiN-CoFe₂ microstructure; (b) Low magnification and (c) high magnification cross-sectional
 335 STEM images; (d) Plan-view STEM images with (e) corresponding EDS mapping of Co, Fe,
 336 Ti, N; (f) High-resolution STEM images of one nanosheet region with ϵ_{yy} strain mapping (g)
 337 and ϵ_{xx} strain mapping (h).

338



339

340 **Fig. 2 | Microstructure turnability of TiN-CoFe₂ nanocomposite thin films.** (a) Schematic

341 drawing of 2Hz TiN-CoFe₂ VAN; (b) Plan-view STEM images of 2Hz TiN-CoFe₂ VAN; (c)

342 Dimension distribution (short edge width and long edge length) of CoFe₂ nanosheets in 2Hz

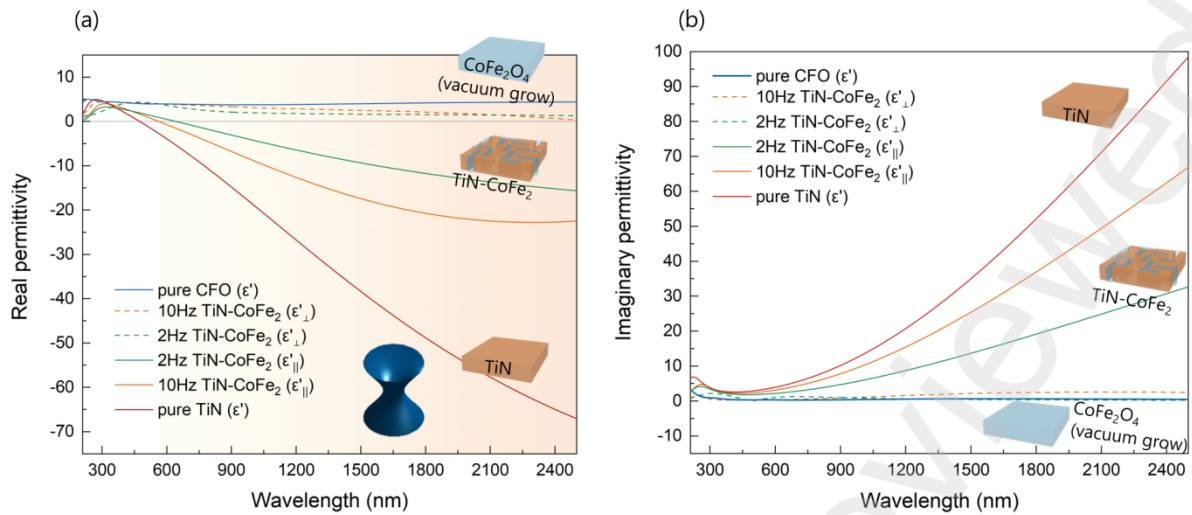
343 sample; (d) Schematic drawing of 10Hz TiN-CoFe₂ VAN; (e) Plan-view STEM images of

344 10Hz TiN-CoFe₂ VAN; (f) Dimension distribution of CoFe₂ nanosheets in 10Hz sample.

345

346

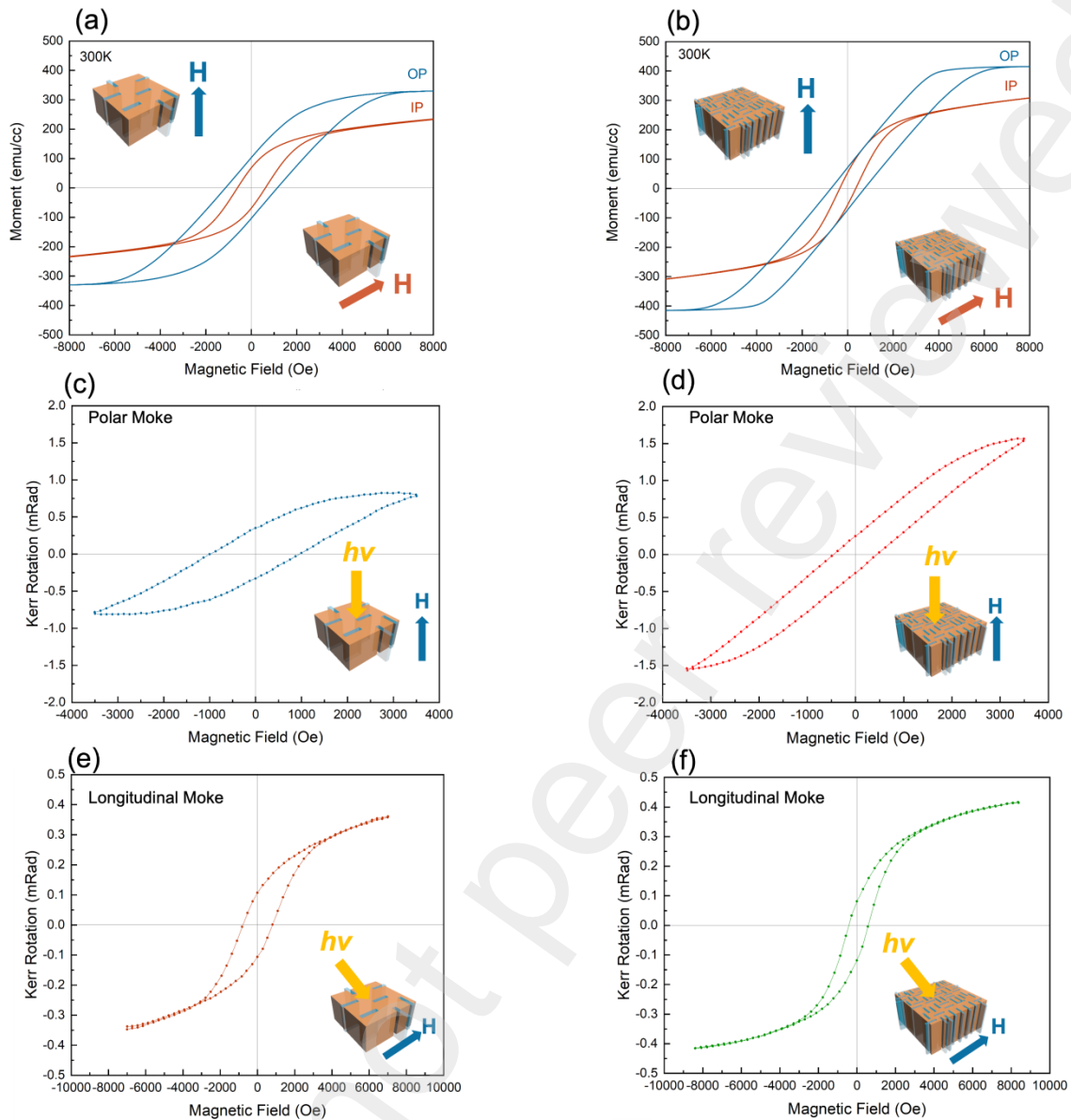
347



348

349 **Fig. 3 | Optical properties of TiN-CoFe₂ nanocomposite thin films.** (a) Real part and (b)
 350 imaginary part of permittivity of 2Hz TiN-CoFe₂, 10Hz TiN-CoFe₂, pure TiN, and pure
 351 CoFe₂O₄ sample.

352



353

354 **Fig. 4 | Magnetic properties and magneto-optical coupling effect in TiN-CoFe₂**

355 **nanocomposite thin films.** (a) Comparison of in-plane and out-of-plane M-H hysteresis loops

356 of 2Hz TiN-CoFe₂ nanocomposites; (b) Comparison of in-plane and out-of-plane M-H

357 hysteresis loops of 10Hz TiN-CoFe₂ nanocomposites; (c) Polar and (e) longitudinal Kerr

358 rotation of 2Hz TiN-CoFe₂ nanocomposites; (d) Polar and (f) longitudinal Kerr rotation of

359 10Hz TiN-CoFe₂ nanocomposites.

360

361

362 References

- 363 [1] D.R. Smith, J.B. Pendry, M.C.K. Wiltshire, *Metamaterials and Negative Refractive Index*,
364 2004. <https://www.science.org>.
- 365 [2] V.M. Shalaev, *Optical negative-index metamaterials*, 2007.
366 www.nature.com/naturephotonics.
- 367 [3] N. Kinsey, C. DeVault, A. Boltasseva, V.M. Shalaev, *Near-zero-index materials for photonics*,
368 *Nat Rev Mater.* 4 (2019) 742–760. <https://doi.org/10.1038/s41578-019-0133-0>.
- 369 [4] A. Poddubny, I. Iorsh, P. Belov, Y. Kivshar, *Hyperbolic metamaterials*, *Nat Photonics.* 7
370 (2013) 958–967. <https://doi.org/10.1038/nphoton.2013.243>.
- 371 [5] P. Shekhar, J. Atkinson, Z. Jacob, *Hyperbolic metamaterials: fundamentals and applications*,
372 *Nano Converg.* 1 (2014). <https://doi.org/10.1186/s40580-014-0014-6>.
- 373 [6] J.B. Khurgin, A. Boltasseva, *Reflecting upon the losses in plasmonics and metamaterials*,
374 *MRS Bull.* 37 (2012) 768–779. <https://doi.org/10.1557/mrs.2012.173>.
- 375 [7] G. v. Naik, V.M. Shalaev, A. Boltasseva, *Alternative plasmonic materials: Beyond gold and*
376 *silver*, *Advanced Materials.* 25 (2013) 3264–3294.
377 <https://doi.org/10.1002/adma.201205076>.
- 378 [8] P. Patsalas, N. Kalfagiannis, S. Kassavetis, *Optical properties and plasmonic performance*
379 *of titanium nitride*, *Materials.* 8 (2015) 3128–3154.
380 <https://doi.org/10.3390/ma8063128>.
- 381 [9] W.P. Guo, R. Mishra, C.W. Cheng, B.H. Wu, L.J. Chen, M.T. Lin, S. Gwo, *Titanium Nitride*
382 *Epitaxial Films as a Plasmonic Material Platform: Alternative to Gold*, *ACS Photonics.* 6
383 (2019) 1848–1854. <https://doi.org/10.1021/acsphotonics.9b00617>.
- 384 [10] C.C. Chang, J. Nogan, Z.P. Yang, W.J.M. Kort-Kamp, W. Ross, T.S. Luk, D.A.R. Dalvit, A.K.
385 Azad, H.T. Chen, *Highly Plasmonic Titanium Nitride by Room-Temperature Sputtering*, *Sci*
386 *Rep.* 9 (2019). <https://doi.org/10.1038/s41598-019-51236-3>.
- 387 [11] T. Krekeler, S.S. Rout, G. v. Krishnamurthy, M. Störmer, M. Arya, A. Ganguly, D.S.
388 Sutherland, S.I. Bozhevolnyi, M. Ritter, K. Pedersen, A.Y. Petrov, M. Eich, M. Chirumamilla,
389 *Unprecedented Thermal Stability of Plasmonic Titanium Nitride Films up to 1400 °C*, *Adv Opt*
390 *Mater.* 9 (2021). <https://doi.org/10.1002/adom.202100323>.
- 391 [12] H. Reddy, U. Guler, Z. Kudyshev, A. v. Kildishev, V.M. Shalaev, A. Boltasseva, *Temperature-*
392 *Dependent Optical Properties of Plasmonic Titanium Nitride Thin Films*, *ACS Photonics.* 4
393 (2017) 1413–1420. <https://doi.org/10.1021/acsphotonics.7b00127>.
- 394 [13] R. Kamakura, S. Murai, S. Ishii, T. Nagao, K. Fujita, K. Tanaka, *Plasmonic-Photonic Hybrid*
395 *Modes Excited on a Titanium Nitride Nanoparticle Array in the Visible Region*, *ACS Photonics.*
396 4 (2017) 815–822. <https://doi.org/10.1021/acsphotonics.6b00763>.
- 397 [14] L. Gui, S. Bagheri, N. Strohofeldt, M. Hentschel, C.M. Zgrabik, B. Metzger, H. Linnenbank,
398 E.L. Hu, H. Giessen, *Nonlinear Refractory Plasmonics with Titanium Nitride Nanoantennas*,
399 *Nano Lett.* 16 (2016) 5708–5713. <https://doi.org/10.1021/acs.nanolett.6b02376>.
- 400 [15] E. Shkondin, T. Repän, O. Takayama, A. v. Lavrinenko, *High aspect ratio titanium nitride*

- trench structures as plasmonic biosensor, *Opt Mater Express*. 7 (2017) 4171. <https://doi.org/10.1364/ome.7.004171>.
- [16] W. Li, U. Guler, N. Kinsey, G. v. Naik, A. Boltasseva, J. Guan, V.M. Shalaev, A. v. Kildishev, Refractory plasmonics with titanium nitride: Broadband, *Advanced Materials*. 26 (2014) 7959–7965. <https://doi.org/10.1002/adma.201401874>.
- [17] G. v. Naik, B. Saha, J. Liu, S.M. Saber, E.A. Stach, J.M.K. Irudayaraj, T.D. Sands, V.M. Shalaev, A. Boltasseva, Epitaxial superlattices with titanium nitride as a plasmonic component for optical hyperbolic metamaterials, *Proc Natl Acad Sci U S A*. 111 (2014) 7546–7551. <https://doi.org/10.1073/pnas.1319446111>.
- [18] J. Huang, D. Zhang, H. Wang, Epitaxial TiN/MgO multilayers with ultrathin TiN and MgO layers as hyperbolic metamaterials in visible region, *Materials Today Physics*. 16 (2021) 100316. <https://doi.org/10.1016/j.mtphys.2020.100316>.
- [19] J. Huang, X. Wang, N.L. Hogan, S. Wu, P. Lu, Z. Fan, Y. Dai, B. Zeng, R. Starko-Bowes, J. Jian, H. Wang, L. Li, R.P. Prasankumar, D. Yarotski, M. Sheldon, H.T. Chen, Z. Jacob, X. Zhang, H. Wang, Nanoscale Artificial Plasmonic Lattice in Self-Assembled Vertically Aligned Nitride–Metal Hybrid Metamaterials, *Advanced Science*. 5 (2018). <https://doi.org/10.1002/advs.201800416>.
- [20] X. Wang, J. Jian, S. Diaz-Amaya, C.E. Kumah, P. Lu, J. Huang, D.G. Lim, V.G. Pol, J.P. Youngblood, A. Boltasseva, L.A. Stanciu, D.M. O’carroll, X. Zhang, H. Wang, Hybrid plasmonic Au-TiN vertically aligned nanocomposites: a nanoscale platform towards tunable optical sensing †, (2019). <https://doi.org/10.1039/c8na00306h>.
- [21] X. Wang, J. Jian, Z. Zhou, C. Fan, Y. Dai, L. Li, J. Huang, J. Sun, A. Donohue, P. Bermel, X. Zhang, H.T. Chen, H. Wang, Self-Assembled Ag–TiN Hybrid Plasmonic Metamaterial: Tailorable Tilted Nanopillar and Optical Properties, *Adv Opt Mater*. 7 (2019) 1–9. <https://doi.org/10.1002/adom.201801180>.
- [22] X. Wang, X. Ma, E. Shi, P. Lu, L. Dou, X. Zhang, H. Wang, Large-Scale Plasmonic Hybrid Framework with Built-In Nanohole Array as Multifunctional Optical Sensing Platforms, *Small*. 16 (2020) 1–10. <https://doi.org/10.1002/sml.201906459>.
- [23] J. Huang, X. Wang, D. Li, T. Jin, P. Lu, D. Zhang, P.T. Lin, H.T. Chen, J. Narayan, X. Zhang, H. Wang, 3D Hybrid Plasmonic Framework with Au Nanopillars Embedded in Nitride Multilayers Integrated on Si, *Adv Mater Interfaces*. 7 (2020) 1–9. <https://doi.org/10.1002/admi.202000493>.
- [24] L. Li, L. Sun, J.S. Gomez-Diaz, N.L. Hogan, P. Lu, F. Khatkhatay, W. Zhang, J. Jian, J. Huang, Q. Su, M. Fan, C. Jacob, J. Li, X. Zhang, Q. Jia, M. Sheldon, A. Alù, X. Li, H. Wang, Self-assembled epitaxial Au-oxide vertically aligned nanocomposites for nanoscale metamaterials, *Nano Lett*. 16 (2016) 3936–3943. <https://doi.org/10.1021/acs.nanolett.6b01575>.
- [25] J. Huang, X.L. Phuah, L.M. McClintock, P. Padmanabhan, K.S.N. Vikrant, H. Wang, D. Zhang, H. Wang, P. Lu, X. Gao, X. Sun, X. Xu, R. Edwin García, H.T. Chen, X. Zhang, H. Wang, Core-shell metallic alloy nanopillars-in-dielectric hybrid metamaterials with magneto-plasmonic

- 441 coupling, *Materials Today*. 51 (2021) 39–47.
442 <https://doi.org/10.1016/j.mattod.2021.10.024>.
- 443 [26] J. Huang, L. Li, P. Lu, Z. Qi, X. Sun, X. Zhang, H. Wang, Self-assembled Co-BaZrO₃
444 nanocomposite thin films with ultra-fine vertically aligned Co nanopillars, *Nanoscale*. 9
445 (2017) 7970–7976. <https://doi.org/10.1039/c7nr01122a>.
- 446 [27] D. Zhang, Z. Qi, J. Jian, J. Huang, X.L. Phuah, X. Zhang, H. Wang, Thermally Stable Au-BaTiO₃
447 Nanoscale Hybrid Metamaterial for High-Temperature Plasmonic Applications, *ACS Appl*
448 *Nano Mater.* 3 (2020) 1431–1437. <https://doi.org/10.1021/acsanm.9b02271>.
- 449 [28] D. Zhang, S. Misra, J. Jian, P. Lu, L. Li, A. Wissel, X. Zhang, H. Wang, Self-Assembled BaTiO₃-
450 Au xAg_{1-x} Low-Loss Hybrid Plasmonic Metamaterials with an Ordered “nano-Domino-like”
451 Microstructure, *ACS Appl Mater Interfaces*. 13 (2021) 5390–5398.
452 <https://doi.org/10.1021/acsami.0c19108>.
- 453 [29] J. Lu, R.L. Paldi, Y. Pachaury, D. Zhang, H. Wang, M. Kalaswad, X. Sun, J. Liu, X.L. Phuah,
454 X. Zhang, A.A. El-Azab, H. Wang, Ordered Hybrid Metamaterial of La_{0.7}Sr_{0.3}MnO₃-Au
455 Vertically Aligned Nanocomposites Achieved on Templated SrTiO₃ Substrate, 2021.
- 456 [30] R. Liang, P. Dosanjh, D.A. Bonn, D.J. Baar, J.F. Carolan, W.N. Hardy, Growth and properties
457 of superconducting YBCO single crystals, 1992.
- 458 [31] S.E. Shirsath, X. Liu, Y. Yasukawa, S. Li, A. Morisako, Switching of magnetic easy-axis using
459 crystal orientation for large perpendicular coercivity in CoFe₂O₄ thin film, *Sci Rep.* 6 (2016)
460 1–11. <https://doi.org/10.1038/srep30074>.
- 461 [32] M. Zheng, X.C. Wu, B.S. Zou, Y.J. Wang, Magnetic properties of nanosized MnFe O particles,
462 1998.
- 463 [33] A. Chen, N. Poudyal, J. Xiong, J.P. Liu, Q. Jia, Modification of structure and magnetic
464 anisotropy of epitaxial CoFe₂O₄ films by hydrogen reduction, *Appl Phys Lett.* 106 (2015).
465 <https://doi.org/10.1063/1.4915504>.
- 466 [34] C.Y. Kuo, Z. Hu, J.C. Yang, S.C. Liao, Y.L. Huang, R.K. Vasudevan, M.B. Okatan, S. Jesse,
467 S. v. Kalinin, L. Li, H.J. Liu, C.H. Lai, T.W. Pi, S. Agrestini, K. Chen, P. Ohresser, A. Tanaka,
468 L.H. Tjeng, Y.H. Chu, Single-domain multiferroic BiFeO₃ films, *Nat Commun.* 7 (2016).
469 <https://doi.org/10.1038/ncomms12712>.
- 470 [35] J.M. Moreau, C. Michel, R. Gerson, W.J. James, FERROELECTRIC BiFeO₃ X-RAY AND
471 NEUTRON DIFFRACTION STUDY, Pergamon Press, 1971.
- 472 [36] B. Zhang, J. Huang, J. Jian, B.X. Rutherford, L. Li, S. Misra, X. Sun, H. Wang, Tuning magnetic
473 anisotropy in Co-BaZrO₃ vertically aligned nanocomposites for memory device integration,
474 *Nanoscale Adv.* 1 (2019) 4450–4458. <https://doi.org/10.1039/c9na00438f>.
- 475 [37] X. Gao, L. Li, J. Jian, H. Wang, M. Fan, J. Huang, X. Wang, H. Wang, Vertically Aligned
476 Nanocomposite BaTiO₃:YMnO₃ Thin Films with Room Temperature Multiferroic Properties
477 toward Nanoscale Memory Devices, *ACS Appl Nano Mater.* 1 (2018) 2509–2514.
478 <https://doi.org/10.1021/acsanm.8b00614>.
- 479 [38] H. Zheng, J. Wang, S.E. Lofland, Z. Ma, L. Mohaddes-Ardabili, T. Zhao, L. Salamanca-Riba,
480 S.R. Shinde, S.B. Ogale, F. Bai, D. Viehland, Y. Jia, D.G. Schlom, M. Wuttig, A. Roytburd, R.

481 Ramesh, Multiferroic BaTiO₃-CoFe₂O₄ Nanostructures, *Science* (1979). 303 (2004) 661–
482 663. <https://doi.org/10.1126/science.1094207>.

483 [39] X. Wang, Z. Qi, J. Liu, H. Wang, X. Xu, X. Zhang, H. Wang, Strong Interfacial Coupling of
484 Tunable Ni–NiO Nanocomposite Thin Films Formed by Self-Decomposition, *ACS Appl Mater*
485 *Interfaces*. (2021). <https://doi.org/10.1021/acsami.1c09793>.

486 [40] B. Zhang, M. Kalaswad, B.X. Rutherford, S. Misra, Z. He, H. Wang, Z. Qi, A.E. Wissel, X. Xu,
487 H. Wang, Au-Encapsulated Fe Nanorods in Oxide Matrix with Tunable Magneto-Optic Coupling
488 Properties, *ACS Appl Mater Interfaces*. 12 (2020) 51827–51836.
489 <https://doi.org/10.1021/acsami.0c14424>.

490 [41] D.A.M.J.L.G.P.H.C.H.-J.L.G. P. M. Voyles*, Atomic-scale imaging of individual dopant atoms
491 and clusters in highly n-type bulk Si, (n.d.).

492 [42] R. Erni, H. Heinrich, G.Z. Kostorz ETH, Quantitative characterisation of chemical
493 inhomogeneities in Al-Ag using high-resolution Z-contrast STEM, 2003.

494 [43] D.O. Klenov, S. Stemmer, Contributions to the contrast in experimental high-angle annular
495 dark-field images, *Ultramicroscopy*. 106 (2006) 889–901.
496 <https://doi.org/10.1016/j.ultramic.2006.03.007>.

497 [44] X. Wang, H. Wang, J. Jian, B.X. Rutherford, X. Gao, X. Xu, X. Zhang, H. Wang, Metal-Free
498 Oxide-Nitride Heterostructure as a Tunable Hyperbolic Metamaterial Platform, *Nano Lett.* 20
499 (2020) 6614–6622. <https://doi.org/10.1021/acs.nanolett.0c02440>.

500 [45] X. Wang, X. Ma, E. Shi, P. Lu, L. Dou, X. Zhang, H. Wang, Large-Scale Plasmonic Hybrid
501 Framework with Built-In Nanohole Array as Multifunctional Optical Sensing Platforms, *Small*.
502 16 (2020) 1–10. <https://doi.org/10.1002/sml.201906459>.

503